AGU PUBLICATIONS

Water Resources Research

RESEARCH ARTICLE
10.1002/2017WR020799

Key Points:
- Developed a terrain-based downscaling procedure applicable to fractional snow covered area products to derive fine resolution binary snow
- Downscaling procedure takes into account both terrain-based accumulation and ablation effects and balances them using a weight factor
- The method can be applied to downscale 500 m fractional snow covered area data to 30 m and to 3 m, scales relevant to ecohydrology research

Correspondence to:
N. C. Cristea,
cristn@u.washington.edu

Citation:
Cristea, N. C., I. Breckheimer, M. S. Raleigh, J. HilleRisLambers, and J. D. Lundquist (2017), An evaluation of terrain-based downscaling of fractional snow covered area data sets based on LiDAR-derived snow data and orthoimagery, *Water Resour. Res.*, *53*, 6802–6820, doi:10.1002/2017WR020799.

Received 20 MAR 2017
Accepted 7 JUL 2017
Accepted article online 13 JUL 2017
Published online 12 AUG 2017

An evaluation of terrain-based downscaling of fractional snow covered area data sets based on LiDAR-derived snow data and orthoimagery

Nicoleta C. Cristea[1], Ian Breckheimer[2], Mark S. Raleigh[3,4], Janneke HilleRisLambers[2], and Jessica D. Lundquist[1]

[1]Civil and Environmental Engineering, University of Washington, Seattle, Washington, USA, [2]Department of Biology, University of Washington, Seattle, Washington, USA, [3]Cooperative Institute for Research in Environmental Science (CIRES), University of Colorado, Boulder, Colorado, USA, [4]National Snow and Ice Data Center (NSIDC), University of Colorado Boulder, Boulder, Colorado, USA

Abstract Reliable maps of snow-covered areas at scales of meters to tens of meters, with daily temporal resolution, are essential to understanding snow heterogeneity, melt runoff, energy exchange, and ecological processes. Here we develop a parsimonious downscaling routine that can be applied to fractional snow covered area (fSCA) products from satellite platforms such as the Moderate Resolution Imaging Spectroradiometer (MODIS) that provide daily ~500 m data, to derive higher-resolution snow presence/absence grids. The method uses a composite index combining both the topographic position index (*TPI*) to represent accumulation effects and the diurnal anisotropic heat (*DAH*, sun exposure) index to represent ablation effects. The procedure is evaluated and calibrated using airborne-derived high-resolution data sets across the Tuolumne watershed, CA using 11 scenes in 2014 to downscale to 30 m resolution. The average matching *F* score was 0.83. We then tested our method's transferability in time and space by comparing against the Tuolumne watershed in water years 2013 and 2015, and over an entirely different site, Mt. Rainier, WA in 2009 and 2011, to assess applicability to other topographic and climatic conditions. For application to sites without validation data, we recommend equal weights for the *TPI* and *DAH* indices and close *TPI* neighborhoods (60 and 27 m for downscaling to 30 and 3 m, respectively), which worked well in both our study areas. The method is less effective in forested areas, which still requires site-specific treatment. We demonstrate that the procedure can even be applied to downscale to 3 m resolution, a very fine scale relevant to alpine ecohydrology research.

1. Introduction

Remotely sensed snow covered area (SCA) data sets with both high spatial and temporal resolutions are needed for research, planning, and management of hydrologic and ecologic resources. MODIS platforms provide daily snow data at a nominal ~500 m resolution, which have been applied in hydrologic studies [*Parajka and Blöschl*, 2008; *Finger et al*., 2011; *Franz and Karsten*, 2013], and reservoir management modeling [*McGuire et al*., 2006], as well as to analyze effects of burned forests on snow [*Micheletty et al*., 2014]. However, higher spatial resolution data are more suitable to support hydrologic modeling and understand subpixel snow spatial heterogeneity for accurate runoff prediction [*Luce at al*., 1999; *Lundquist and Dettinger*, 2005; *Clark et al*., 2011]. Distributed hydrologic modeling is often applied at 30 to 100 m resolution, with patchy snow affecting the energy balance feedback [*Liston*, 1995, 1999]. Larger-scale modeling requires parameterization of subgrid-scale variability [*Liston*, 2004], which is often included in the form of snowmelt depletion curves [*Shamir and Georgakakos*, 2007]. Ecologists are also particularly interested in high spatial and temporal resolution snow data, critical for studying alpine plant communities. In mountain systems, plant diversity and phenological events such as growing and flowering, are directly related to snow cover extent and snow duration [*Choler*, 2005; *Venn et al*., 2011; *Ford et al*., 2013; *CaraDonna et al*. 2014], and are highly variable over small spatial scales (m and tens of m), as a function of terrain features and microclimate [e.g., *Little et al*., 1994; *Rochefort et al*., 1994]. Remotely sensed snow covered area (SCA) data sets have the potential to inform studies investigating these linked snow-ecology processes

[*Tappeiner et al*., 2001; *Carlson et al*., 2015; *Dedieu et al*., 2016], but both high temporal and spatial resolutions are needed to accurately determine snow duration at the scale needed for plant ecology research [*Dedieu et al*., 2016].

Ideally, for evaluating fine-scale spatial snow patterns, we would use high-resolution data sets such as LiDAR-derived snow depth data, orthophotography, or IKONOS imagery [e.g., *Czyzowska-Wisniewski et al*., 2015], but these high-resolution products are either not always available, too expensive, or too infrequent to effectively track the evolution of snow cover over time. Of all the available satellite products, MODIS-based (and going forward, VIIRS) products come closest to meeting the temporal resolution required for estimating snow disappearance dates for research and applications, providing global daily snapshots at a resolution of ~500 m. Recent research has demonstrated that this coarse spatial scale can be refined through downscaling, which is assigning presence/absence snow data on higher-resolution grids based on the coarse-scale MODIS-derived fractional snow cover area (fSCA) products [*Walters et al*., 2014; *Li et al*., 2015].

Previously developed downscaling methods have been primarily based on ablation drivers of snow cover spatial variability. *Walters et al*. [2014] used topographic radiation-derived slope factors and elevation, while *Li et al*. [2015] used air temperature and solar radiation combined in a degree-day approach to downscale MODIS fSCA to 30 m resolution. However, snow accumulation processes are at least as important as ablation processes in determining the date of snow disappearance [see *Raleigh and Lundquist*, 2012]. Terrain features drive snow variability [*Geddes et al*., 2005; *Jost et al*., 2007; *Anderson et al*., 2014], with variable wind [*Hiemstra et al*., 2002; *Winstral et al*., 2013] and vegetation effects as a function of climate, vegetation type, and local conditions [*Lundquist et al*., 2013; *Dickerson-Lange et al*. 2015a,b]. Slope and aspect were also found important for both accumulation and the duration of the snowpack [*López-Moreno et al*., 2014].

Here, we build on previous approaches and propose a modified downscaling method that incorporates both ablation and accumulation effects on snow spatial variability. To account for spatial variability in accumulation processes, our method uses the topographic position index [*Weiss*, 2001], *TPI*, to identify areas of depressions and fissures in the landscape. Statistical analyses of snow depth data have identified the topographic position index (*TPI*), a measure of the relative position of a digital elevation model (DEM) grid cell in a given neighborhood to the mean elevation of that neighborhood [*Weiss*, 2001], as the strongest explanatory variable of snow depth spatial variability [*Revuelto et al*., 2014]. A terrain-derived index combining slope and aspect, the diurnal anisotropic heat (*DAH*) index, described in detail in section 3.2, is used to identify areas where snow is likely to disappear first (ablation effects). The *DAH*, accounts also for differential warming on different aspects, which is important for snow spatial variability during the ablation season [*Jost et al*., 2007; *Revuelto et al*., 2014; *Anderson et al*., 2014]. We derive these two indices from a higher-resolution DEM and combine them to inform the spatial distribution of binary snow based on fSCA values from the coarser resolution grids. Our study specifically aims to:

1. Evaluate and test the new downscaling routine to map seasonal snow from fractional snow cover area (fSCA) products across multiple years and regions.
2. Evaluate the downscaled results separately over forested and exposed areas, and
3. Downscale to very fine spatial resolution (3 m) over both areas (the scale at which many organisms operate—and thus of interest to ecohydrology).

We focus our analysis on two different geographic regions: (1) the upper Tuolumne River Watershed, CA, and, (2) Mount Rainier, WA. We evaluate the method using the 2014 Tuolumne snow data, and demonstrate that the procedure is robust when applied over the same area in different years, 2013 and 2015. We then apply the method over the Mt. Rainier area, which has different topography and very different climatic conditions, to test for spatial transferability of our method for downscaling from 500 m resolution to 30 and 3 m resolutions.

We use a framework based on airborne-derived (LiDAR and orthoimagery) high-resolution snow data sets. We derive 500 m-scale fSCA from the high-resolution binary data (snow presence/absence) for input to the downscaling routine. These inputs are more certain than satellite-derived imagery, which could be affected by the topographic and sensor-viewing angle effects, and are uncertain over forested areas [*Raleigh et al*., 2013; *Rittger et al*., 2013]. This ensures that we focus our testing on the skill of the downscaling methodology, when provided with reliable input data. The downscaling method can be applied to any existing

MODIS-based (or VIIRS-based) fSCA products [e.g., *Salomonson and Appel*, 2004; *Painter et al*., 2009], and can be automated and used routinely by users to develop high-resolution maps of the seasonal progression of snowmelt in complex terrain (see Appendix B). We describe the study sites in section 2, and the methods (downscaling framework, method, and testing scenarios) in section 3. We present the results in section 4. Finally, we discuss the results and summarize the conclusions in sections 5 and 6.

2. Study Areas

2.1. Tuolumne Watershed, California

The upper Tuolumne River watershed is located on the western slopes of the Sierra Nevada, California (Figure 1a). It spans about ~3000 m in elevation, covering an area of 1190 km^2 above the Hetch Hetchy reservoir. Complex features characterize the landscape. The higher elevation areas are covered by granitic bedrock and shallow, erodible soils, while the subalpine areas are forested with interspersed meadows.

The climate is Mediterranean, with mild winter temperatures, low annual precipitation, and warm and dry summers. The area receives most of the precipitation as snow, which gradually melts during the ablation season, with the snow line retreating by about 300 m every 2–3 weeks [*Rice et al*., 2011]. The snowpack develops from only about 5–7 storms [*Lundquist et al*., 2015], and the difference between a low and a high snowpack is given by only a few storm events. About 36% of the watershed is forested, mostly by lodgepole pine (*Pinus contorta*) and red fir (*Abies magnifica*). According to Parameter-elevation Relationships on Independent Slopes Model (PRISM) [Daly *et al*., 2008; *Daly et al*., 1994] climatology, annual precipitation averages 800–1500 mm range. Middle elevations (2100–3000 m) hold most of the snow and provide 40–60% of the snowmelt, whereas the high elevations (above 3000 m) contribute with about 30–40% [*Rice et al*., 2011]. At the Tuolumne Meadows snow pillow site (37.6°N, 119.7°W, 2600 m), monthly minimum temperature ranges from −12°C in winter to 1–3°C in summer, whereas the maximum monthly temperatures vary between 4–5°C and 22°C.

Beginning in 2013, the watershed was surveyed each melt season, as part of the NASA Jet Propulsion Laboratory Airborne Snow Observatory (ASO) program [*Painter et al*., 2016], with the main purpose to quantify the amount of water stored in the snowpack for water management. In this study, we use the 2013–2015 ASO data. Paleoclimate records over the Sierra Nevada Mountains showed that the 2012–2015 period was characterized by pronounced drought, with an exceptionally low snowpack in 2015, exceeding the 95th percentile for a 500 year return period [*Belmecheri et al*., 2016]. The snowpacks in 2014 and 2015 were also

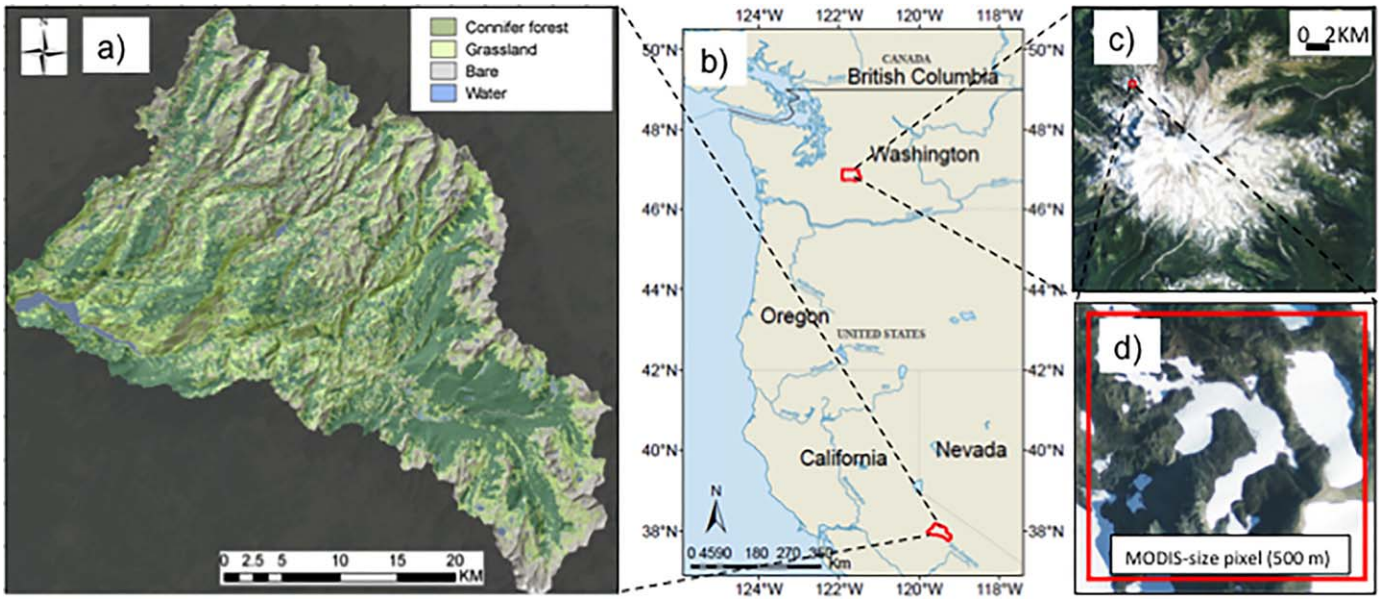

Figure 1. (a) Tuolumne River watershed, CA; (b) locations of Tuolumne River watershed, CA and Mt. Rainier, WA; (c) snow cover as captured by orthoimagery 16 August 2011, and (d) example of the spatial distribution of snow covered areas across the surface of a MODIS pixel on Mt. Rainier (red square).

the lowest over a 31 year long period (1985–2015), based on analyzing peak snow water equivalent (SWE) climatology derived from the Landsat 5–8 imagery [*Margulis et al*., 2016].

2.2. Mount Rainier, Washington

The Mount Rainier National Park area, located in the Cascade Mountains of the United States (Figure 1b), covers a topographically complex and large elevation gradient (600–4390 m) with heterogeneous snow cover. Between the lowest and the highest elevation weather stations located in the Park, the mean annual precipitation varies from 1905 mm (at 579 m) to 3200 mm (at 1646 m), respectively. The region's climate is Maritime, with dry summers and very wet winters, making the snowpack on Mt. Rainier significant. The climate is influenced by the proximity to the Pacific Ocean and varies with elevation. Precipitation falls unevenly across the Mt. Rainier area, with the wettest areas at higher elevations and on the westward side of the mountain due to orographic and storm track effects. Permanent ice and snow cover an area of about 90.6 km^2, mostly at elevations above 2100 m. The area is frequently cloud-covered, with July and August being the sunniest months of the year when the highest temperatures vary between 15 and 20°C. Most of the Mt. Rainier forest is coniferous. Douglas fir (*Pseudotsuga menziesii*) and hemlock (*Tsuga canadensis*) dominate the lower elevations, whereas subalpine fir (*Abies lasiocarpa*) can be found at higher elevations.

We selected two National Agriculture Imagery Program (NAIP) orthophotos (3 August 2009 and 16 August 2011) that provide an opportunity to assess snow mapping at high spatial resolutions across the area. NAIP acquires 1 m resolution data during the agricultural growing season every 3 years. These images can capture late season snow over high mountains, such as the Mt. Rainier. Cooler temperatures than usual characterized the summer of 2011 due to strong La Niña influences. Total snowfall in 2011 was also significant, ranking at the 93rd percentile over the 1920–2016 period. These conditions allowed the snow to be present at lower elevations at the time the NAIP imagery was acquired. Total snowfall in 2009 was also relatively large, ranking at the 78th percentile over the same 1920–2016 period. In both images, the snow line is above tree line (∼2000 m). Figure 1c shows the snow-covered areas over Mt. Rainier during the 16 August 2011 NAIP survey, while Figure 1d illustrates snow cover variability within one MODIS pixel as a function of terrain features.

3. Methods

3.1. Testing Framework

We take advantage of reliable, platform-independent fine-scale SCA data derived from high-resolution (1–3 m) airborne orthophotography and from fine-scale snow (3 m) depth data collected using light detection and ranging (LiDAR) technology. Such data sets exist over a number of watersheds, including our study areas. In the United States, LiDAR-derived snow data are collected as part of the ASO program beginning in 2013 within the Tuolumne area, and the program is expanding over other regions [*Painter et al*., 2016]. A dual-laser system was used (Riegl LMS-Q1560, with pulse rates up to 800 kHz, and a 60° field of view, distinguishing multiple targets per pulse), with increased capabilities to detect snow in forested areas [*Painter et al*., 2016]. Although relatively infrequent, airborne orthoimagery capturing late season snow is available through local or national programs such as NAIP.

Because satellite-derived products are subject to cloud contamination and positional uncertainty, and cannot resolve individual trees, there are several advantages to using orthoimagery or LiDAR-derived data, rather than satellite-derived data, to evaluate a downscaling procedure. Less uncertainty exists in both the input and validation data, as the baseline fSCA can be determined with higher accuracy and higher resolution from orthoimagery or LiDAR-derived snow data. This allows us to isolate errors due to the downscaling procedure alone and to test the downscaling at resolutions higher than 30 m, which is valuable for ecological studies.

The testing framework consists of the following steps: (1) derivation of high-resolution 30 and 3 m binary snow/no-snow from the LiDAR-derived snow depth data (Tuolumne area) and orthophotography (Mt. Rainier area), (2) reconstruction of MODIS-scale (∼500 m) fSCA using data from the previous step, (3) downscaling of the 500 m fSCA data to spatially explicit binary maps, and (4) comparison of the downscaled results with the data from step 1). These steps are illustrated in Figure 2 for the Tuolumne area.

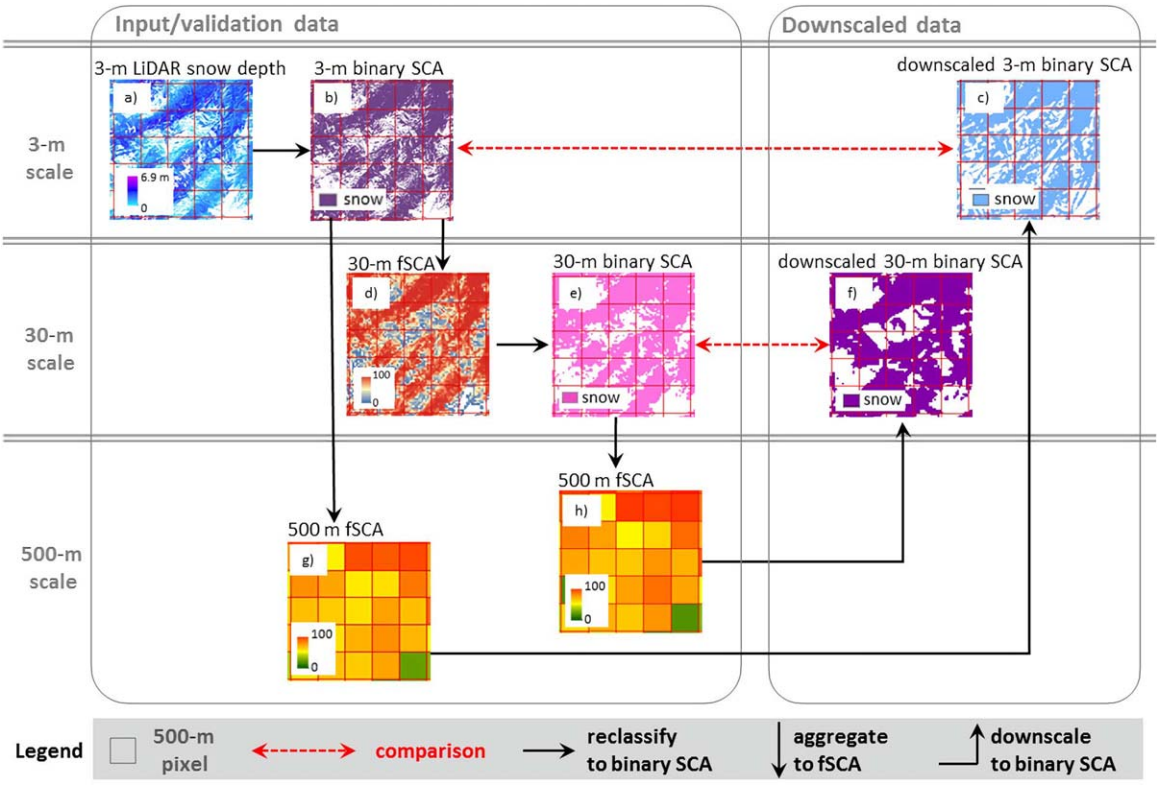

Figure 2. Framework and workflow for downscaling at 30 m scale and 3 m scale. Figures shown on 2 May 2014 for a subset of the Tuolumne watershed.

Over the Tuolumne area, the 3 m binary snow data were generated from the 3 m snow depth data using a 3 cm threshold, to account for uncertainty in the LiDAR accuracy (reported 1 cm in *Painter et al*. [2016]) and for effects of grass and small rocks (Figures 2a and 2b). There were then aggregated to the 30 m scale to estimate 30 m fSCA (Figure 2d), as an intermediate step. A 50% pixel snow coverage threshold was applied to the 30 m fSCA to derive 30 m binary snow data (Figure 2e). Over the Mt. Rainier area, snow cover was delineated by aggregating the 1 m resolution imagery to 3 m-resolution to reduce noise, summing digital numbers for the red, green, and near-infrared bands (min = 0, max = 765 after summation), and then thresholding the resulting map to produce a binary map of snow presence and absence. In these images, the blue band was discarded because it showed reduced contrast due to atmospheric scattering. We chose a brightness threshold, rather than a more sophisticated classification method, because snow surfaces are at or near the maximum brightness in this imagery. This means that clean snow surfaces were nearly completely separated from other surfaces by their brightness, and few pixels had intermediate values, creating a distinct minimum in the image band histogram. We used this histogram minimum (value 590) as a threshold for separating snow and nonsnow surfaces. A visual assessment showed that using this histogram minimum as a threshold reliably distinguished clean snow from the background.

3.2. Downscaling Procedure

The downscaling algorithm assigns presence/absence snow data to a higher-resolution grid based on the likelihood of snow presence informed by a composite topographic index and fSCA from a coarser resolution grid (e.g., ~500 m for a MODIS size pixel). Our composite index is a linear combination of independently derived terrain indices balancing representations of ablation and accumulation effects:

$$SVI = DAH * w + (1 - w) * TPI, \quad (1)$$

where *SVI* (−) is the snow variability index, *DAH* (−) is the diurnal anisotropic heating index [*Böhner and Antonić*, 2009], used to represent ablation effects, *TPI* (−) is the topographic position index [*Weiss*, 2001] used to represent accumulation effects, and *w* is a calibrated weighting factor. Snow water equivalent, SWE, was found to relate with terrain curvature (which is similar in concept with the *TPI*) at near-peak

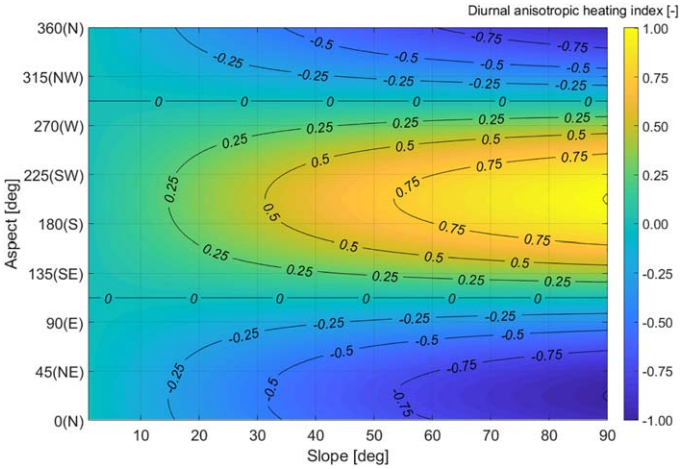

Figure 3. Diurnal anisotropic heating index variation as a function of slope and aspect.

snow accumulation [*Sexstone and Fassnacht*, 2014]. The diurnal anisotropic heating index, *DAH*, developed for the Northern Hemisphere, takes into account both slope and aspect and is calculated as:

$$DAH = cos(\alpha_{max} - \alpha) * arctan(\beta), \quad (2)$$

where $\alpha_{max} = 202.5°$ (SSW) is the slope aspect receiving the maximum amount of heat, α is the slope aspect, and β is the slope angle in radians. *DAH* is highest on steep southwest-facing slopes (that have higher afternoon temperatures than east facing slopes for the same amount of received solar radiation), and lowest values on steep north-facing slopes. *DAH* (Figure 3) ranges from -1 to 1 and is zero on flat terrain. *DAH* is therefore considered here as an indicator of both the effects of temperature and topographic solar radiation that control differential snowmelt on particular slopes: snow disappears first on the southeast, south, and southwest facing slopes and lasts longer on the northeast, north, and northwest facing slopes. Snowmelt on south-facing slopes is likely to be more sensitive to increases in temperature [*López-Moreno et al*., 2014].

The topographic position index, *TPI*, represents an indicator of a given pixel's position relative to the mean elevation of a defined surrounding area/neighborhood:

$$TPI = z_0 - \bar{z}, \quad \text{with } \bar{z} = \frac{1}{n_R} \sum_{i \in R} z_i, \quad (3)$$

where z_0 is the elevation of the given cell, and $\bar{z}$ is the average elevation of the neighborhood containing R number of cells.

Negative *TPI* indicates that the pixel is lower than the neighborhood average elevation, whereas positive indicates that the pixel is higher than the average. *TPI* values vary with the size and shape of the neighborhood. Spatial relationships of *DAH* and *TPI* with snow distribution patterns across a mountainous landscape (Mt. Rainier area) are exemplified in Figures 4c–4n at two different spatial scales: hundreds of meters, region 1, Figures 4c–4h (e.g., MODIS scale) and tens of meters, region 2, Figures 4i–4n (e.g., Landsat scale). In Figure 4, terrain indices *DAH* and *TPI* (estimated as in *Jenness* [2006], using a 27 m circular neighborhood) were derived using a 3 m DEM data set collected during the September 2007 to October 2008 period, and provided for this study by the National Park Service (NPS).

The snow variability index, *SVI* (equation (1)), has the highest values on steep, insolated slopes, and lowest values in concavities and depressions. The *SVI* pixels are ranked from low to high within the area of the coarser pixel; then the highest ranked pixels (i.e., lowest *SVI*) are assigned "snow" such that fSCA over the area of each coarser resolution pixel is preserved. Both *DAH* and *TPI* are normalized for each of the coarser pixel area prior to calculating *SVI*, making the *SVI* range from 0 to 1. The method's sensitivities to the weight factor *w* and to the neighborhood size and shape for *TPI* are further explored in section 4.

3.3. Performance Metrics

We use the *F* score derived using contingency table metrics for binary data [*Olson and Delen*, 2008] as an overall measure of matching performance, accounting for both commission and omission errors. For each image, we determine *true negatives* (*TN*) as the number of pixels that are snow-free in both downscaled and validation data, *false positives* (*FP*) as the number of "snow" pixels present only in downscaled but not in the validation image, *false negatives* (*FN*) as the number of "snow" pixels present in the validation data but not in the downscaled product, and *true positives* (TP) as the "snow" pixels common in both downscaled and validation data sets. The *F* score is then estimated as:

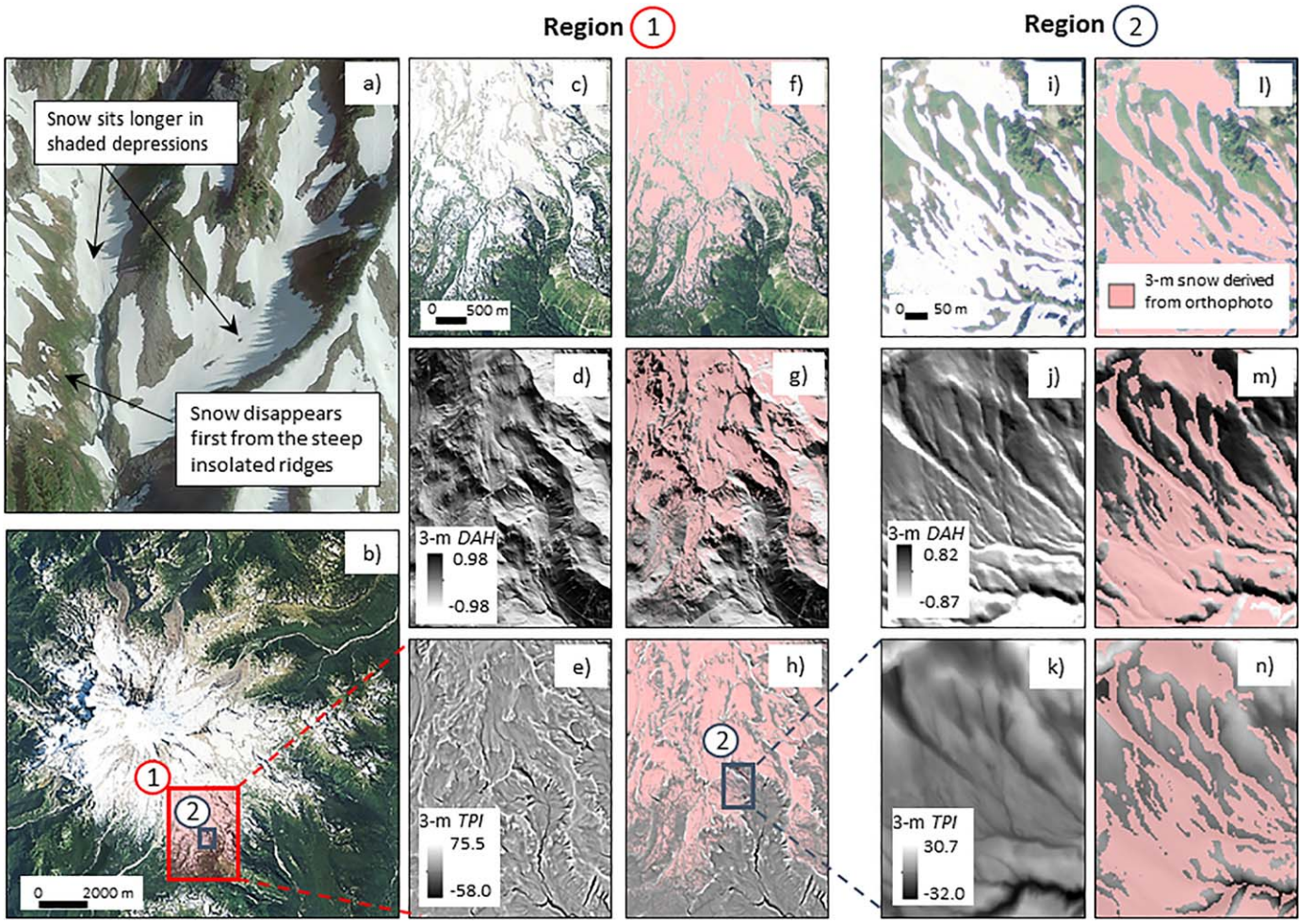

Figure 4. (a) Example illustration of Google Earth image of snow patterns in complex terrain over a representative area on Mt. Rainier; (b) orthophoto from 16 August 2011 of Mt. Rainier; (c) Zoomed-in orthophoto for region (box) 1 in Figure 4b; (d) diurnal anisotropic index (*DAH*) distribution over region 1; (e) topographic position index (*TPI*) over region 1; (f, g h) snow cover derived from the orthophoto overlaid over the image to the left; (i–n) corresponding plots as Figures 4c–4h, but for region 2 (smaller box). All grids are shown at 3 m spatial resolution. *TPI* was derived using a circular neighborhood and 27 m searching radius.

$$F = \frac{2TP}{2TP + FP + FN} \tag{4}$$

We complement the *F* score results with the *Kappa* statistic [*Cohen*, 1960] to determine how the accuracy of the downscaled product compares with the accuracy of a random chance assignment, as defined below:

$$Kappa = \frac{totalAccuracy - randomAccuracy}{1 - randomAccuracy} \tag{5}$$

where:

$$totalAccuracy = \frac{TP + TN}{TP + TN + FP + FN} \tag{6}$$

$$randomAccuracy = \frac{(TN + FP) * (TN + FN) + (FN + TP) * (FP + TP)}{(TP + TN + FP + FN) * (TP + TN + FP + FN)}, \tag{7}$$

where *totalAccuracy* is the observational probability of agreement and *randomAccuracy* is a hypothetical expected probability of agreement. According to *Landis and Koch* [1977], *Kappa* higher than 0.80 are considered near perfect agreement, 0.61–0.80, strong, 0.41–0.60 moderate, 0.21–0.40, fair, and less than 0.20 poor. Both *F* score and *Kappa* metrics range from 0 to 1, with 1 indicating the best matching scores.

3.4. Testing Scenarios

We evaluate the procedure for downscaling at 30 m resolution as a function of the weight *w*, and *TPI* neighborhood size and shape. We use the Tuolumne 2014 data, which had the most scenes over the melt season (11), for model development. We test the sensitivity to ablation and accumulation representation, inclusion of wind effects, and uncertainty in fSCA input. The weight was varied between 0 (accumulation only) and 1 (ablation only), in 0.1 increments, defining the relative representation of the two processes in equation (1). We tested both circular and rectangular *TPI* neighborhoods, with searching distances varying between 60 and 180 m. Prior downscaling methods have used radiation or estimated radiation in complex terrain [*Li et al*., 2015; *Walters et al*., 2014], whereas we use a terrain-derived index that does not require computationally intensive models of incident radiation. We evaluate our method's performance when using more comprehensive estimates of radiation instead of *DAH*, by sequentially replacing *DAH* in equation (1) with: (1) average season radiation (day of year 50–150), (2) 7 day average radiation prior to the day of survey, as the approximate time interval between the ASO flights and also used in prior analyses [e.g., *Revuelto et al*., 2014], and (3) slope factors (as in *Walters et al*. [2014]). In all cases, potential shortwave radiation accounting for topographic shading was estimated for clear sky conditions as a function of terrain slopes and aspects [*Fu and Rich*, 2000, 2002].

In addition to terrain features, snow accumulation patterns are also driven by the direction of storms and orographic effects. To test for wind deposition effects, we multiply the wind parameter α_r [*Böhner and Antonić*, 2009] by the *TPI* in equation (1):

$$SVI = DAH * w + (1-w) * \alpha_r * TPI, \tag{8}$$

The wind parameter α_r ranges from 0.7 (leeward) to 1.3 (windward), and takes into account direction of the prevailing winds, as well as the influence of distant terrain on wind sheltering [*Böhner and Antonić*, 2009; *Gerlitz et al*., 2015]. Equation (8) was inspired by equation ((5).3), pg. 221 in *Böhner and Antonić* [2009] (Appendix A), that combines α_r with curvature and elevation in an intuitively constructed index indicative of snow accumulation based on a similar combination originally developed by *Brown* [1994]. In both the Mt. Rainer and Tuolumne areas, most winter storms come from the southwest. We evaluate the matching performance when using equation (8) relative to the southwest direction.

The matching scores are also likely to be affected by the uncertainty in the fSCA input. Here, we test the sensitivity of the matching performance to the uncertainty in input data by using fSCA reconstructed from two different grids and methods. We use fSCA derived from binary 30 and 3 m data, using neighborhood statistical techniques and using Gaussian pyramid reduction techniques (as in *Bair et. al*. [2016]).

After the best model configuration is chosen based on the 2014 Tuolumne data, this configuration is then applied to the 2013 (6 scenes) and 2015 data (10 scenes) to evaluate the method's performance in different water years. Results are then evaluated separately on forested and exposed areas over the Tuolumne area. Finally, we evaluate the method's performance over the Mt. Rainier area and discuss the method's transferability across different climates and mountain systems, and additionally evaluate downscaling at very high spatial resolution (3 m) in both areas (sections 4.1.4 and 4.2).

4. Results

4.1. Method Evaluation, Tuolumne River Watershed

4.1.1. Downscaling to 30 m Resolution: Sensitivity to Weight and *TPI* Neighborhood

The weight *w* and the *TPI* circular neighborhood size have variable effects on the downscaling efficiency as a function of day of year and snow cover variability (Figure 5). The overall *F* and *Kappa* scores for downscaling to 30 m spatial resolution over the Tuolumne watershed for 7 April 2014 (beginning of the survey scene, 71% snow covered) and 5 May 2014 (midseason, 42% snow covered) are higher than those for 31 May and 5 June 2014 (toward the end of the season, 13% and 8.7% and snow covered, respectively), when less snow was on the ground (Figure 5). The method is less sensitive to the weight *w* and *TPI* size on days that had higher fSCA values, for which the algorithm has a generally smaller chance to incorrectly map the snow.

Both ablation and accumulation processes are important in the downscaling routine, and their relative relevance varies as a function of day-of-year and overall percentage of snow cover across the watershed (Figure 5). For example, including accumulation effects earlier in the season has a smaller impact than later in the

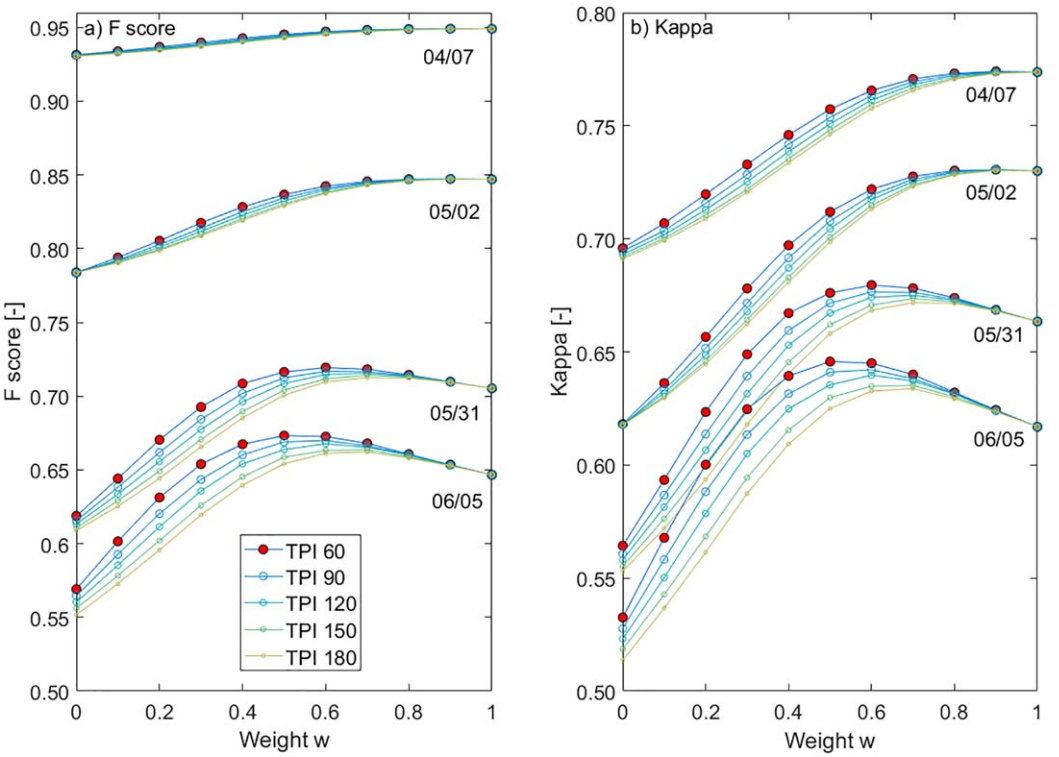

Figure 5. (a) *F* scores and (b) *Kappa* scores for downscaling at 30 m resolution as a function of weight *w* and circular *TPI* size for 4 days in 2014. *TPI* searching distance is expressed in meters; $w = 0$ means *TPI* controls the distribution, and $w = 1$ means *DAH* controls the distribution.

season when snow cover is patchy, and the only remaining snow is found in cirques, depressions, or fissures. Two contrasting examples illustrate the above observations. On 7 April 2014, the overall *F* score varied between 0.95 and 0.93, with an average of 0.94 across all *w*'s and *TPI*'s tested. On 5 May 2014, the second to last day of the survey, the *F* score varied between 0.61 and 0.72, with an average of 0.68 (Figure 5a).

The most effective *TPI* neighborhood size was 60 m, meaning that the closer vicinity terrain data were most important to detect higher and lower point locations needed to distribute snow. For a given weight *w*, the spread between *F* scores for a range of *TPI* neighborhood sizes was higher for days with patchy snow (see an example for 5 June, Figure 5a). The most effective weight (for which the *F* scores were highest in most days, except for 5 June) was 0.7. For *TPI* radius = 60 m and $w = 0.7$, the most effective overall combination, the average *F* score for all days was 0.83, whereas for $w = 0.5$ the average score was very close, equal to 0.82. The average scores decreased to 0.8 for $w = 0.3$, and down to 0.76 for $w = 0$ (accumulation only). The scores were more sensitive to the weight values than the *TPI* neighborhood size, and especially for late-season observations, when the accumulation effects mattered more. As an example, for the last day, 5 June, the most effective weight was 0.5. These late-season downscaling results are also the most important for representing late summer streamflow and for supporting ecology research.

Kappa tests for all 11 days in 2014 rejected the null hypothesis of random assignment at 95% confidence level (i.e., observed agreement was not accidental). Similar to the *F* scores, the *Kappa* scores are higher earlier in the season (Figure 5b). Most *Kappa* scores fell into the strong agreement category (0.61–0.8), with the exception of four values (for $w < 0.4$ on 31 May and 5 June 2014) that fell into the moderate agreement category (0.41–0.6). *Kappa* estimates the degree of agreement with a random classifier, and gives a relative measure of how the system accuracy compares with expected accuracy. All *Kappa* scores for $w = 0.7$ fell into the strong agreement category. Influences of circular versus rectangular areas for *TPI* were also explored, and they were similar at weights of 0.6 and 0.7 (because ablation mattered more than *TPI*).

4.1.2. Sensitivity to Ablation and Accumulation Representation and Wind Effects

When comparing different representations of ablation effects, the highest matching scores were estimated when using the diurnal anisotropic heating index, *DAH* (as in equation (1)), with an average *F* score of 0.83

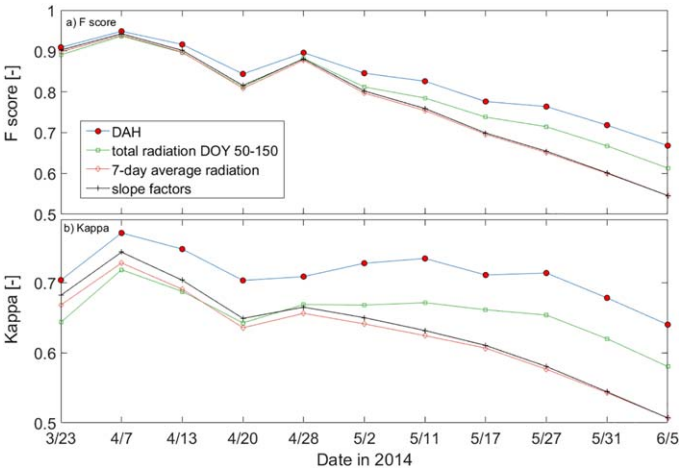

Figure 6. (a) *F* scores and (b) *Kappa* scores for downscaling at 30 m resolution using different representation of ablation effects: (1) diurnal anisotropic heating (*DAH*) index, (2) total radiation for days of year DOY 50–150, (3) 7 day average radiation prior to day of survey and, (4) slope factors.

for all 11 days in 2014 (Figure 6a). The next best options were season average (day of year 50–150) solar radiation (average score 0.80) and slope factors (average score 0.77). A similar implementation as in *Walters et al*. [2014], using both slope factors and elevation, provided an average score of 0.76. Most *Kappa* scores were within the (0.61–0.8) interval (Figure 6b), with greater divergence between methods later in the season. We tested elevation (as in *Walters et al*. [2014]) by sequentially replacing it in equation (1) for *DAH* and *TPI*, and the scores were lower each time (0.75 and 0.73, respectively). Because *DAH* performed best, we use it for the remaining of the tests as described below.

The inclusion of wind effects (equation (8)) made overall very little difference (third digit) in each of the individual *F* scores for the 11 days in 2014. However, even this small difference varied with day of the year, with slight improvements earlier in the season, when two major important snowfall events occurred, and slight reductions later in the season when melt is accelerated, and snow cover is patchier and highly controlled by terrain features. Wind effects did not have a significant impact on the model performance. Therefore we removed the wind contribution and continued with the original formulation (equation (1)). Replacing *TPI* with total curvature in equation (1) provided very similar results, making *TPI* and curvature interchangeable in equation (1).

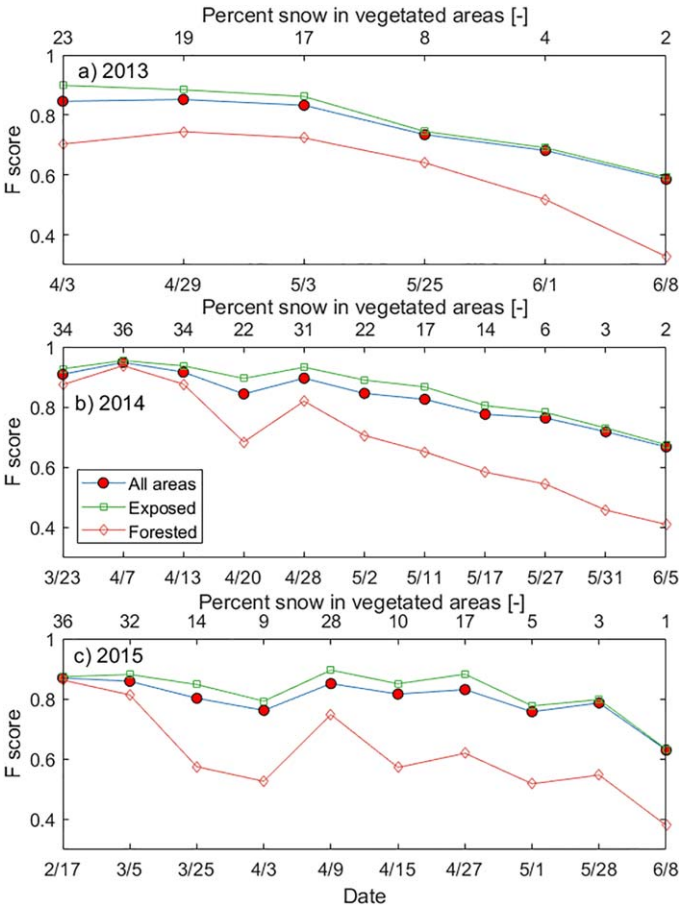

Figure 7. *F* scores for evaluating forested and exposed areas separately during (a) 2013, (b) 2014 and, (c) 2015.

4.1.3. Vegetation Effects

To investigate vegetation effects, we downscaled all scenes in 2013, 2014 and 2015 and estimated binary metrics separately for forested and nonforested areas. All runs applied equation (1) configured for *TPI* with a search radius of 60 m and $w = 0.7$. The method performed worse in forested than in exposed areas (Figure 7). For days when the percentage of snow in forested areas was below 20%, the *F* score dropped below 0.6, and as low as 0.3, albeit for cases when very little snow remained in the forest (less than 5–6%). The *Kappa* scores were also lower.

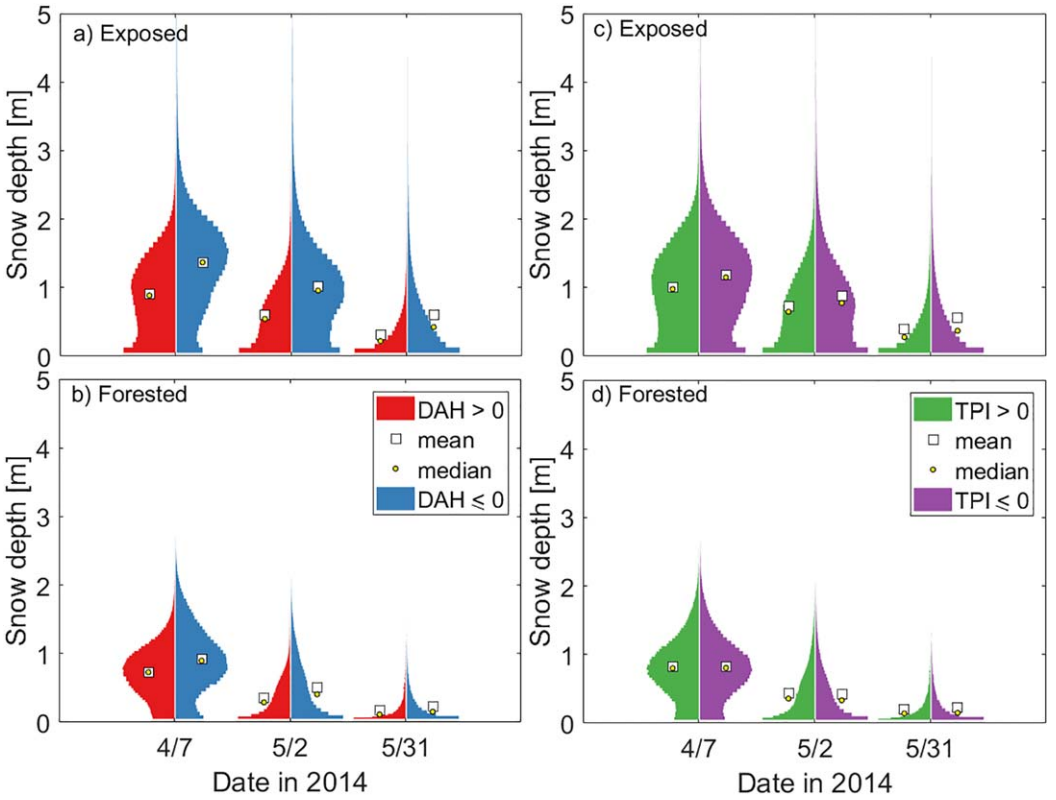

Figure 8. Distributions of snow depth for three days in 2014 (at the beginning, middle, and end of the snowmelt season) for: (a) exposed and (b) forested areas as a function of diurnal anisotropic heating index, *DAH*, (c) exposed and (d) forested areas as a function of 60 m circular neighborhood topographic position index *TPI*.

The different model performance in forested versus exposed areas is most likely explained by the differences in snow accumulation and snowmelt patterns, and the inability of the *SVI* to capture these differences. Figure 8 shows the different 30 m snow depth distributions for forests versus exposed areas as a function of *TPI* and *DAH* on three dates in 2014. Snow depth is higher in the depressions and on north facing slopes (negative *TPI*, negative *DAH*) and lower on the ridges and on south facing slopes (positive *TPI*, positive *DAH*), illustrating the terrain control on snow cover variability in both areas. The differences (as tested using Wilcoxon rank sum tests with bootstrapping at 95% confidence level) remain distinct as the ablation season progresses, demonstrating terrain influence on snow cover variability. However, terrain features exert a greater control on snow depth variability in exposed compared with forested areas (Figure 8), which explains why the downscaling techniques perform better in exposed areas. The differences are also greater earlier in the season, which may explain why the *F* scores are higher at these times.

4.1.4. Downscaling to 3 m Resolution

When downscaling to 3 m resolution, a *TPI* with a 27 m searching distance provided the best matching *F* scores (Figure 9). However, for $w = 0.7$, the most effective weight, the *F* scores for all *TPI* options varied within the second digit. The matching scores were similar to the 30 m downscaling, demonstrating the method's robustness to downscaling at very high spatial resolutions (meters). All *Kappa* scores showed strong agreement (0.61–0.8).

4.2. Method Transferability, Mt. Rainier Area

We applied the best configuration from Tuolumne ($w = 0.7$ and *TPI* radius = 60 m) to the Mt. Rainier area. For this direct transfer, the *F* score was 0.71 in 2011, similar to the summer results from Tuolumne. The scores improved with changing the parameters (*w* and *TPI* size), with the best score 0.03 higher (for $w = 0.2$ and *TPI* radius = 120 m) than the direct transfer. For this most effective weight, the variation in score for various *TPI* circular sizes was only 0.003. The average *F* score for all weights and *TPI* considered was 0.72 for the circular neighborhood, and 0.71 for the rectangular neighborhood, but with a larger spread in *F* score, 5.6%.

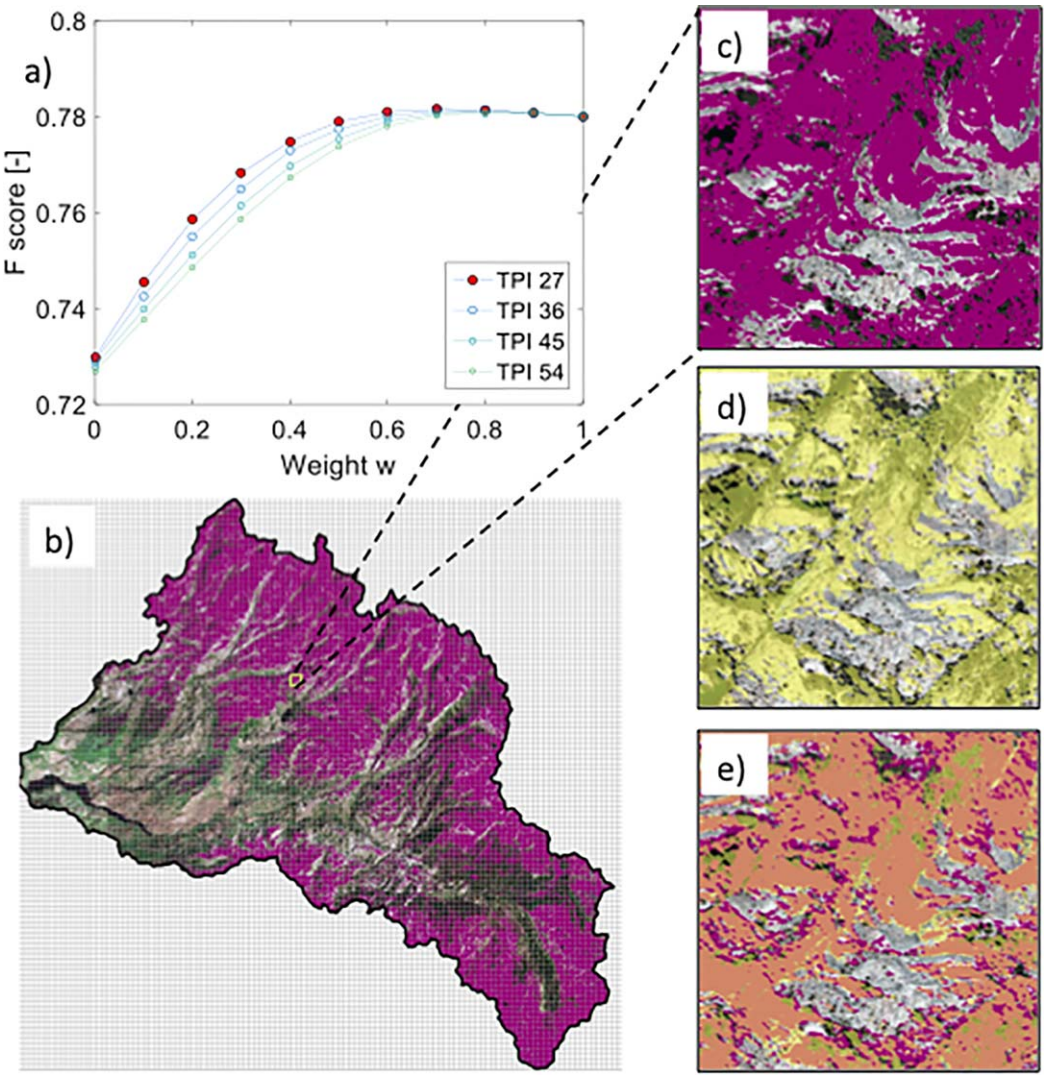

Figure 9. (a) *F* scores for downscaling to 3 m resolution as a function of weight *w* and *TPI* searching distance in meters, with $w = 0$ meaning *TPI* controls the distribution and $w = 1$ meaning no weight on the *TPI*, (b) spatial distribution of 3 m downscaled snow covered areas for *TPI* 27 m (pink color), (c) zoomed-in downscaled map (pink color), (d) zoomed-in snow covered areas derived from snow depth (yellow color), (e) zoomed-in overlaid maps from Figures 9c and 9d, where orange represents snow in both, pink represents downscaled snow that was not observed, yellow represents observed snow that was not downscaled, and clear (underlying rock and forest) represent no snow in either. The zoomed-in area is approximately four MODIS pixels (~2 km on a side). Data shown for 2 May 2014.

The lowest score was 0.67 (for $w = 1$). The *F* score was more sensitive to the weight factor *w* than the *TPI* neighborhood size. Downscaling to 3 m resolution with direct transfer ($w = 0.7$, *TPI* = 27 m) provided an *F* score of 0.68, which was improved to 0.72 with setting the weight to 0.2, and only marginally improved when using larger *TPI* neighborhoods. For $w = 0.5$ and *TPI* radius = 27 m, the score was 0.70. Similar patterns were observed for the 2009 data, which, although about 2 weeks earlier in the season, had 20% less snow. All *Kappa* scores for all the tests showed good agreement.

5. Discussion

5.1. Basic Approach

Topography drives not only solar loading, but also accumulation patterns and wind redistribution effects, with snow persisting longer in topographic concavities [*Hiemstra et al.*, 2002; *Sturm and Wagner*, 2010]. Here, we propose a downscaling method to derive snow presence/absence data from fractional snow covered data products based on topographic effects on both snow accumulation and melt patterns. To account

for accumulation effects, our method uses the topographic position index, *TPI*, a measure of a relative position of a DEM pixel in a given neighborhood [*Weiss*, 2001]. *Revuelto et al*. [2014] found that *TPI*, along with terrain curvature, correlated best with snow depth amongst several other terrain-derived indices, with the strength of the correlation varying as a function of day of the year, elevation range, and topographic complexity in the designated neighborhood. Larger neighborhoods are more likely to reveal larger-scale terrain features such as valleys and ridges, while smaller neighborhoods more likely identify local depressions/fissures [*De Reu et al*., 2013]. Ranges of *TPI* variation over specific areas and DEM resolutions are indicative of topographic complexity at various scales. As an example, the standard deviation of all *TPI* values (derived from 30 m DEMs with a search radius of 60 m) was three times larger over the entire Tuolumne area than over the Mt. Rainier area, indicating higher topographic complexity. Curvature was equally effective index as the *TPI*, as both attempt to identify concave and convex areas across the landscape. However, the *TPI* has a simpler and more intuitive construction and proved effective in describing snow depth variability with predictive power in modeling both snow [*Revuelto et al*., 2014; *Carlson et al*., 2015] and plant species distributions [*Guisan et al*., 1999].

Our downscaling method uses the terrain-derived diurnal anisotropic index, *DAH*, to represent shortwave radiation effects on snow cover variability. While this seems a simplified approach, *DAH* performed better in our tests than when using topographically distributed effects of potential shortwave radiation. We attribute this better performance to the higher weighting in *DAH* of the west-facing slopes compared with the similarly sloped east-facing slopes. The west-facing slopes have increased afternoon temperatures, generating additional available heat for melt. In contrast, daily total topographic radiation is equal on both east and west-facing slopes. The *DAH* captures the increased probability of snow being ripe and ready to melt in the afternoon, when sun hits west-facing slopes, than in the morning, when the sun hits east-facing slopes, without requiring detailed and computationally intensive complete snow energy-balance modeling.

The inclusion of larger-scale wind effects in our procedure did not significantly improve the matching performance. With consistent synoptic weather, terrain features make snow distribution patterns similar from year to year [*Sturm and Wagner*, 2010; *Deems et al*., 2008; *Schirmer et al*., 2011], where storms from the prevailing wind direction provide similar peak accumulation patterns [*Schirmer and Lehning*, 2011; *Prokop and Procter*, 2016]. Wind plays a role in the larger-scale (hundreds of m) snow deposition patterns through preferential deposition on certain mountain slopes [*Lehning et al*., 2008; *Gerlitz et al*. 2015]. At smaller spatial scales (m to tens of m), wind could shift the snow as a function of local terrain [*Winstral and Marks*, 2002; *Mott and Lehning*, 2010], likely transporting more snow to the depressions. Here, we focused on mapping snow-covered areas (rather than snow depth), especially during ablation season when snow is disappearing and patchy. The wind effect during this period was likely represented to some extent through the accumulation component in the snow variability index (equation (1)). Convex areas are generally more exposed to wind than the concave areas that trap the windblown snow, and the *TPI* likely captured the effect of snow transported from ridge tops and into topographic concavities. We did not find an improvement when including more detailed wind effects, such as windward versus leeward slopes.

5.2. Method Application

5.2.1. Effect of Weight

Properly weighting the two ablation and accumulation components defining the snow variability index (equation (1)) is important for improving snow mapping through downscaling, as a function of local conditions and processes dominating the energetics of snowmelt. Over the Mt. Rainier area, ablation effects were less important to mapping snow-covered areas than in the Tuolumne area, as the most effective weight was 0.2, compared with 0.7. In Tuolumne, snowmelt is driven mostly by shortwave radiation [*Marks and Dozier*; 1992; *Lundquist and Flint*, 2006], and less by longwave radiation, which is more important earlier in the season [*Marks and Dozier*, 1992]. Also earlier in the season, clouds are more important for producing precipitation than impacting snowmelt [*Sumargo and Cayan*, 2017]. The Mt. Rainier area is significantly more cloud-covered during spring and summer (as noted from the *Wilson and Jetz* [2016] data set), when clouds reduce shortwave incoming radiation and emit additional longwave radiation contributing to snowmelt. The snowpack of Mt. Rainier is also deeper and lasts longer in the wider depressions; therefore accumulation effects mattered more. These effects were likely exaggerated by our choice of years: Our Tuolumne study years were dry and warm (greater melt effects), while our Mt. Rainier study years were cool and wet (greater accumulation effects). The influence of the weight and *TPI* effects in time can be noticed

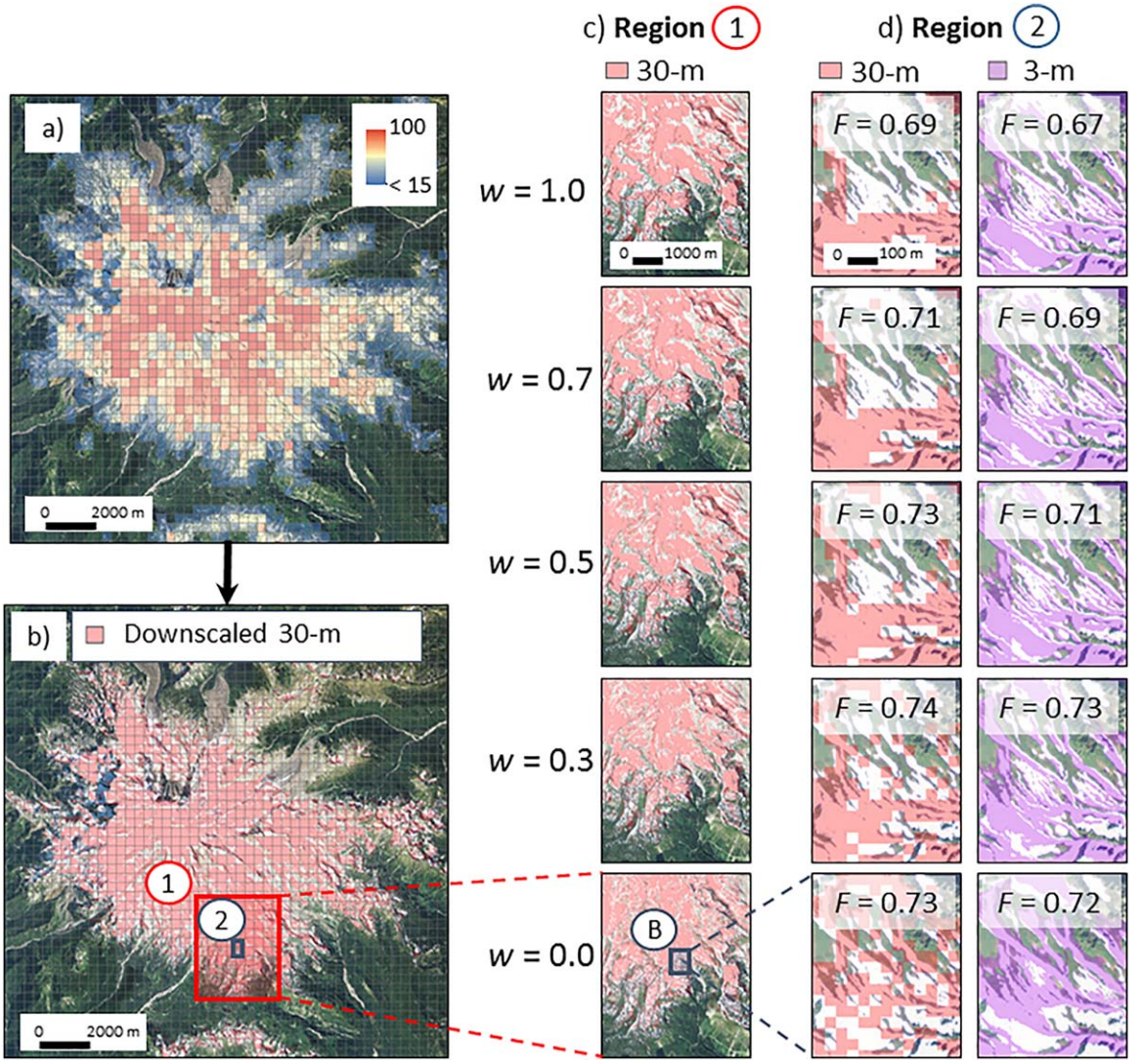

Figure 10. (a) Reconstructed 500 m fSCA spatial distribution over the Mt. Rainier area on 16 August 2011; (b) Binary 30 m downscaled SCA for $w = 0.2$, *TPI* 60 m; (c) Binary 30 m downscaled SCA for *TPI* 60 m and different weights, shown for region 1 (rows); (d) First column: same as in Figure 10c, but for region 2; (d) second column: same as in Figure 10d first column, but downscaled at 3 m resolution. *F* scores shown in columns (c) and (d) are computed for the entire area in Figure 10b.

in Figure 5 for the Tuolumne area. As the ablation season progresses, *TPI* represents better the snow trapped in concavities. This is consistent with patterns of LiDAR-derived snow depth in the Tuolumne area (Figure 8c), as well as with patterns observed in other geographic settings, where deeper snow was found in areas with concave curvature during the ablation season [e.g., *Sold et al*., 2013].

Spatial patterns of downscaled binary snow maps vary as a function of weight. This is exemplified in Figure 10 that shows downscaled binary snow maps at both 3 and 30 m spatial resolutions for five different weights for visual examination of the differences over the Mt. Rainier area. Larger snow-covered areas are mapped using ablation representation alone ($w = 1$ in equation (1)), but this misses existing snow in smaller depressions (Figures 10c and 10d, top row). This is more evident for the 30 m scale than for the 3 m scale. By increasing accumulation effects (decreasing w), the algorithm more successfully maps the snow in the finer terrain depressions (Figure 10d). Statistics for the 3 m downscaling were similar or higher than the corresponding 30 m (Figure 10c), showing consistency in results for downscaling at different spatial scales, as well as the robustness of the downscaling algorithm.

5.2.2. Effect of *TPI* Circular Neighborhood Size

Over the Tuolumne area, which is topographically more complex than Mt. Rainier, the most effective *TPI* circular neighborhood for downscaling at 30 m resolution was the 60 m searching distance. In the Mt. Rainier

area, the larger circular neighborhoods (90–150 m) were slightly more efficient (by less than 1% in the *F* scores) than the 60 m neighborhood at the most effective weight. In both areas, the 30 m neighborhoods were almost as efficient as the 60 m neighborhoods, with average *F scores* lower by third digit values than the 60 m. The differences in *F* scores due to using different *TPI* neighborhood sizes were more pronounced for the late season dates, with the *F* score varying within about 3–5% (see example in Figure 5, for 5 June 2014 in Tuolumne). Our method was applied for downscaling to very high spatial resolutions (3 m), with snow distribution at finer scale well represented across terrain features where the physical and ecological processes are highly variable (see example in Figure 10, last column). The larger *TPI* neighborhoods for downscaling to 3 m resolution were also slightly more efficient in the Mt. Rainier area (by only about 0.6% difference in *F* score between 27 and 54 m—we did not see improvements in the matching scores beyond this size), than in the Tuolumne area (27 m). Average *F* scores (for all weights) slightly decrease at both sites for smaller neighborhoods (*TPI* searching distances 9 and 18 m). In the Mt. Rainier area, the differences were more pronounced: the average *F* score decreased by 0.03 between the *TPI* 27 m and *TPI* 9 m search distances. These searching distances are consistent with the grid resolution (i.e., larger searching distances for coarser grids). For comparison, *Revuelto et al*. [2014] identified 25 m as the most effective *TPI* search distance when working with 5 m resolution snow depth grids to describe snow depth variation. At these small spatial scales (meters and tens of meters), microtopography is more important for characterizing snow depth spatial variability [*López-Moreno et al*., 2011], as well as other site-specific processes, such as drifting and preferential deposition or snowfall from cliffs and avalanches [*Clark et al*., 2011].

5.3. Sensitivity to Methodological Decisions in Geospatial Analysis

5.3.1. Circular Versus Rectangular *TPI* Areas

Differences in downscaling performance when using rectangular versus circular *TPI* neighborhoods were observed in both Mt. Rainier and Tuolumne areas. In both regions, differences in *F* scores for the different circular TPI sizes tested were smaller, compared with the rectangular case. Based on these results, we recommend using *TPI* circular neighborhoods with our downscaling method.

5.3.2. Sensitivity to fSCA Input Data

As demonstrated in previous downscaling studies [e.g., *Walters et al*., 2014; *Li et al*., 2015], the matching performance depends on the accuracy of the input data. In this study, we examined this type of uncertainty using different scale grids and methods for fSCA reconstruction. For example, the fSCA data sets reconstructed from the 3 m data differ slightly from those based on 30 m data. At the watershed scale, these differences vary as a function of day of the year and total snow on the ground. For the first six observation days in 2014, the total watershed scale fSCA was larger when reconstructed from the 30 m (Figure 2h) than from the 3 m data (Figure 2g) by 2–11%, with the larger values earlier in the season, whereas for the last 5 days they were smaller by 2–13%, with the larger values toward the end of the season. Both were derived using neighborhood aggregation techniques, but differ in value due to scale and truncation in deriving 30 m binary SCA (Figures 2d and 2e) and edge effects. We used the fSCA data reconstructed from the 30 m data (Figure 2h) as input to the algorithm in all of the 30 m downscaling tests, primarily because the downscaled maps were compared with the 30 m binary data that were generated through truncation. For downscaling at 30 m resolution, the average *F* score varied within 9% for all methods of fSCA reconstruction. This indicates that the input data are of paramount importance for the accuracy of the downscaled snow maps, potentially having more influence on the results than specific choices of model parameters.

5.4. Future Directions

5.4.1. Drier Snow Environments, Wind Effects

In both the Tuolumne and Mt. Rainier areas wind matters more during snowfall, and acts to deposit more snow in the depressions. In a more continental regime (like Colorado) wind factors may be more important between storms than they are in a maritime regime. Applying more refined schemes to represent smaller-scale snowdrift patterns would require detailed descriptions of wind fields [*Schneiderbauer et al*., 2008; *Mott et al*., 2011; *Prokop and Procter*, 2016], which are usually not readily available over large areas in the mountains. Our method performed well in both wet and dry years and in different climatic settings over complex areas with heavy snow, and wind effects were negligible. In our test cases, the varying performance over the season depended on the input fSCA data sets, and other errors associated with the mapping and downscaling routine, as topography cannot fully explain snow variability in complex terrain. *Tappeiner et al*. [2001] showed that about 71–81% uncertainty in snow duration is explained by elevation, slope and aspect,

topographic solar radiation during the winter, number of days with air temperature less than 0°C, and vegetation in a small catchment in the central Alps area. In the Pyrenees, *López-Moreno et al.* [2015] estimated that 50–70% of the snow depth variance at scales from 25 to 99 m was explained by slope, wind effects, subgrid variability in elevation, and potential incoming radiation. Our results are at the upper end of these prediction ranges, with *F* scores for the season averaging of ~0.8. Further tests are needed to know if such skill could be obtained in a dry, continental environment.

5.4.2. Vegetation Effects

Vegetation affects snow distribution across the landscape through interception and other site-specific accumulation and melt patterns [*Jost et al.*, 2007; *Anderson et al.*, 2014; *Cristea et al.*, 2014; *Revuelto et al.*, 2015; *Zheng et al.*, 2016]. Accumulation is usually higher in the open areas, but whether snow persists longer in the forest or in the open is a function of climate, forest type, elevation, and slope [*Lundquist et al.*, 2013; *Ellis et al.*, 2010]. In our method, terrain influence in the vegetated areas only partially explained the spatial distribution of snow cover. The method performed worse in vegetated than in the open areas, especially when very little snow remained in the forest. The model also performed worse when fSCA values were small, affecting the overall downscaling performance. Our reconstructed fSCA estimates ranged from 0 to 100. Existing standard MODIS-based fSCA products [*Salomonson and Appel*, 2004] range from 0 to 100, whereas MODSCAG fSCA values [*Painter et al.*, 2009] range from 15 to 100. MODIS-derived fSCA data in forested areas remain highly uncertain, especially in denser forests [*Raleigh et al.*, 2013], and currently our method does not include any specific treatment of the vegetated areas. However, satellite-derived fSCA estimates in forested areas may improve in the future, and LiDAR-derived snow data can provide support to develop alternative schemes to improve current methods.

5.5. Recommendations for Method Application to Other Regions

Results from downscaling to 30 and 3 m resolution from both the Tuolumne and Mt. Rainier areas showed that variations in *F* scores for different *TPI* sizes at their most effective weights are relatively small, within 1%, and larger up to 2–3% for other weights. Differences in *F* scores are larger, within 15% for the weight factor range of variation (0–1). Examining this variation pattern for both areas, we concluded that using $w = 0.5$ provides good downscaling results without major deductions in *F* scores from the peak values (1% for Tuolumne, and 2% for the Mt. Rainier). Close range neighborhoods proved effective for mapping snow; therefore we recommend using circular *TPI* neighborhoods with 60 and 27 m search radius for downscaling to 30 and 3 m, respectively, combined with a $w = 0.5$ weight factor. The diurnal anisotropic index, *DAH* (equation (2)) is optimized for midlatitudes in the Northern Hemisphere but can be modified for the southern hemisphere, by replacing N with S, and for areas north of the Arctic circle (by reducing the E-W importance).

The results from downscaling MODIS-scale fSCA products for the Tuolumne and Mt. Rainier areas indicate potential for applying the downscaling method to finer spatial scales (meters) using both MODIS-based fSCA products and other SCAG products under current development (30 m, from Landsat platforms). Launched in 2013, Landsat 8 circles the entire Globe every 16 days, and has an 8 day offset to Landsat 7, which can help increase the temporal resolution from the combined Landsat platforms. Successful application of the proposed downscaling technique depends on the quality of both the fSCA and DEM data sets, as well as the ability to coregister the remotely sensed fSCA value with the specific area on the DEM it is looking at. DEM accuracy is especially important for downscaling at high spatial resolutions (meters). The method can be directly applied to other mountain systems in the northern hemisphere using the above default recommendations. If fine-resolution validation data are available for comparison, the method can be further tuned to find the optimal balance between accumulation and ablation representation, and the *TPI* size as a function of terrain complexity. High-resolution data from the newly launched satellites such as Sentinel 2 or 3, and/or data from manual observations and terrestrial laser scans can assist the comparisons.

6. Summary and Conclusions

We use a framework based on airborne-derived high-resolution (3 m) snow data to develop and test a simple terrain-based downscaling technique that uses coarse spatial resolution fractional snow covered area (fSCA) data to derive higher-resolution binary (presence/absence) snow maps. Specifically, our method includes the effects from both accumulation and ablation processes, while previous methods used ablation

effects as the primary driver of snow spatial variability. We use nonsatellite data, with fSCA data and ground validation data derived from high-resolution airborne LiDAR or orthoimagery to reduce uncertainty. We demonstrate that the method is transferable in time (through testing it during three different seasons in the Tuolumne area), and in space (by applying it over the Mt. Rainier area under different climatic conditions). For applicability to different geographic areas, we recommend a balanced representation of ablation and accumulation and close circular neighborhood sizes for deriving the topographic position index (60 and 27 m, for downscaling to 30 and 3 m resolution, respectively). This parameterization can be further refined provided that reliable validation data are available. The method is likely to perform better on exposed and less vegetated areas, such as alpine environments. We show that the procedure can be applied to downscale fractional snow cover products at very high spatial resolutions (3 m).

Appendix A: The Snow Potential Index

The snow potential index (SNOW) defining potential snow accumulation as described in *Böhner and Antonić* [2009], based on *Brown* [1994]:

$$SNOW = \alpha_r \cdot C_{rv} \cdot \frac{z - z_{\min}}{z_{range}},$$

where α_r is the relative land-surface aspect, as a function of aspect and the azimuth of the prevailing wind direction (°), C_{rv} is terrain curvature, and z is elevation (m).

Appendix B: Source Code

The downscaling procedure is coded in Matlab and can be downloaded from the following Github account, along with additional description about the input files using an example from this study: https://github.com/NCristea/Downscale-fractional-snow-covered-area-datasets.

Acknowledgments
We thank the Mountain Hydrology Group for helpful feedback and discussions and Kat Bormann and the Airborne Snow Observatory (ASO) Group at the NASA Jet Propulsion Laboratory for sharing their high-resolution snow depth data products. Tuolumne ASO data can be requested at https://aso.jpl.nasa.gov/. Mt. Rainier orthoimagery is available through https://gdg.sc.egov.usda.gov/. Funding was provided through the NASA grants NNX14AC34G and NNX15AB29G. Raleigh was additionally supported by a CIRES visiting postdoctoral fellowship. We thank two anonymous reviewers and López-Moreno for suggestions to improve the manuscript.

References

Anderson, B. T., J. P. McNamara, H. P. Marshall, and A. N. Flores (2014), Insights into the physical processes controlling correlations between snow distribution and terrain properties, *Water Resour. Res.*, *50*, 4545–4563, doi:10.1002/2013WR013714.

Bair, E. H., K. Rittger, R. E. Davis, T. H. Painter, and J. Dozier (2016), Validating reconstruction of snow water equivalent in California's Sierra Nevada using measurements from the NASA Airborne Snow Observatory, *Water Resour. Res.*, *52*, 8437–8460, doi:10.1002/2016WR018704.

Belmecheri, S., F. Babst, E. R. Wahl, D. W. Stahle, and V. Trouet (2016), Multi-century evaluation of Sierra Nevada snowpack, *Nat. Clim. Change*, *6*(1), 2–3.

Böhner, J., and O. Antonić (2009), Land-surface parameters specific to topo-climatology, *Dev. Soil Sci.*, *33*, 195–226.

Brown, D. G. (1994), Predicting vegetation types at treeline using topography and biophysical disturbance variables, *J. Veg. Sci.*, *5*(5), 641–656.

CaraDonna, P. J., A. M. Iler, and D. W. Inouye (2014), Shifts in flowering phenology reshape a subalpine plant community, *Proc. Natl. Acad. Sci. U. S. A.*, *111*(13), 4916–4921, http://doi.org/10.1073/pnas.1323073111.

Carlson, B. Z., P. Choler, J. Renaud, J. P. Dedieu, and W. Thuiller (2015), Modelling snow cover duration improves predictions of functional and taxonomic diversity for alpine plant communities, *Ann. Bot.*, *116*(6), 1023–1034, doi:10.1093/aob/mcv041.

Choler, P. (2005), Consistent shifts in alpine plant traits along a mesotopographical gradient, *Arct. Antarct. Alp. Res.*, *37*(4), 444–453.

Clark, M. P., J. Hendrikx, A. G. Slater, D. Kavetski, B. Anderson, N. J. Cullen, T. Kerr, E. Örn Hreinsson, and R. A. Woods (2011), Representing spatial variability of snow water equivalent in hydrologic and land-surface models: A review, *Water Resour. Res.*, *47*, W07539, doi:10.1029/2011WR010745.

Cohen, J. (1960), A coefficient of agreement for nominal scales, *Educ. Psychol. Meas.*, *20*(1), 37–46.

Cristea, N. C., J. D. Lundquist, S. P. Loheide, C. S. Lowry, and C. E. Moore (2014), Modelling how vegetation cover affects climate change impacts on streamflow timing and magnitude in the snowmelt-dominated upper Tuolumne Basin, Sierra Nevada, *Hydrol. Processes*, *28*(12), 3896–3918.

Czyzowska-Wisniewski, E. H., W. J. van Leeuwen, K. K. Hirschboeck, S. E. Marsh, and W. T. Wisniewski (2015), Fractional snow cover estimation in complex alpine-forested environments using an artificial neural network. *Remote Sens. Environ.*, *156*, 403–417.

Daly, C., R. P. Neilson, and D. L. Phillips (1994), A statistical-topographic model for mapping climatological precipitation over mountainous terrain, *J. Appl. Meteorol.*, *33*(2), 140–158.

Daly, C., M. Halbleib, J. I. Smith, W. P. Gibson, M. K. Doggett, G. H. Taylor, J. Curtis, and P. P. Pasteris (2008), Physiographically sensitive mapping of climatological temperature and precipitation across the conterminous United States, *Int. J. Climatol.*, *28*(15), 2031–2064.

Dedieu, J. P., B. Z. Carlson, S. Bigot, P. Sirguey, V. Vionnet, and P. Choler (2016), On the importance of high-resolution time series of optical imagery for quantifying the effects of snow cover duration on alpine plant habitat, *Remote Sens.*, *8*(6), 481.

Deems, J. S., S. R. Fassnacht, and K. J. Elder (2008), Interannual consistency in fractal snow depth patterns at two Colorado mountain sites, *J. Hydrometeorol.*, *9*(5), 977–988.

De Reu, J., et al. (2013), Application of the topographic position index to heterogeneous landscapes, *Geomorphology*, *186*, 39–49.

Dickerson-Lange, S. E., J. A. Lutz, K. A. Martin, M. S. Raleigh, R. Gersonde, and J. D. Lundquist (2015a), Evaluating observational methods to quantify snow duration under diverse forest canopies, *Water Resour. Res.*, *51*, 1203–1224, doi:10.1002/2014WR015744.

Dickerson-Lange, S. E., J. A. Lutz, R. Gersonde, K. A. Martin, J. E. Forsyth, and J. D. Lundquist (2015b), Observations of distributed snow depth and snow duration within diverse forest structures in a maritime mountain watershed, *Water Resour. Res.*, *51*, 9353–9366, doi:10.1002/2015WR017873.

Ellis, C. R., J. W. Pomeroy, T. Brown, and J. MacDonald (2010), Simulation of snow accumulation and melt in needle leaf forest environments, *Hydrol. Earth Syst. Sci.*, *14*(6), 925–940.

Finger, D., F. Pellicciotti, M. Konz, S. Rimkus, and P. Burlando (2011), The value of glacier mass balance, satellite snow cover images, and hourly discharge for improving the performance of a physically based distributed hydrological model, *Water Resour. Res.*, *47*, W07519, doi:10.1029/2010WR009824.

Ford, K. R., A. K. Ettinger, J. D. Lundquist, M. S. Raleigh, and J. H. R. Lambers (2013), Spatial heterogeneity in ecologically important climate variables at coarse and fine scales in a high-snow mountain landscape, *PLoS One*, *8*(6), e65008, doi:10.1371/journal.pone.0065008.

Franz, K. J., and L. R. Karsten (2013), Calibration of a distributed snow model using MODIS snow covered area data, *J. Hydrol.*, *494*, 160–175.

Fu, P., and P. M. Rich (2000), *The Solar Analyst 1.0 Manual*, Helios Environ. Model. Inst. (HEMI), Vermont.

Fu, P., and P. M. Rich (2002), A geometric solar radiation model with applications in agriculture and forestry, *Comput. Electron. Agric.*, *37*(1), 25–35, https://doi.org/10.1016/S0168-1699(02)00115–1.

Geddes, C. A., D. G. Brown, and D. B. Fagre (2005), Topography and vegetation as predictors of snow water equivalent across the alpine treeline ecotone at Lee Ridge, Glacier National Park, Montana, USA, *Arct. Antarct. Alp. Res.*, *37*(2), 197–205.

Gerlitz, L., O. Conrad, and J. Böhner (2015), Large-scale atmospheric forcing and topographic modification of precipitation rates over High Asia-a neural-network-based approach, *Earth Syst. Dyn.*, *6*(1), 61–81, doi:10.5194/esd-6-61-2015.

Guisan, A., S. B. Weiss, and A. D. Weiss (1999), GLM versus CCA spatial modeling of plant species distribution, *Plant Ecol.*, *143*(1), 107–122, doi:10.1023/A:1009841519580.

Hiemstra, C. A., G. E. Liston, and W. A. Reiners (2002), Snow redistribution by wind and interactions with vegetation at upper treeline in the Medicine Bow Mountains, Wyoming, USA, *Arct. Antarct. Alp. Res.*, *34*, 262–273.

Jenness, J. (2006), *Topographic Position Index (tpi_jen. avx) Extension for ArcView 3*, x, v. 1.3 a. Jenness Enterprises, Flagstaff, Ariz. [Available at http://www.jennessent.com/arcview/tpi.htm.]

Jost, G., M. Weiler, D. R. Gluns, and Y. Alila (2007), The influence of forest and topography on snow accumulation and melt at the watershed-scale, *J. Hydrol.*, *347*(1), 101–115.

Landis, J. R., and G. G. Koch (1977), The measurement of observer agreement for categorical data, *Biometrics*, *33*(1), 159–174.

Lehning, M., H. Löwe, M. Ryser, and N. Raderschall (2008), Inhomogeneous precipitation distribution and snow transport in steep terrain, *Water Resour. Res.*, *44*, W07404, doi:10.1029/2007WR006545.

Li, H. Y., Y. Q. He, X. H. Hao, T. Che, J. Wang, and X. D. Huang (2015), Downscaling snow cover fraction data in mountainous regions based on simulated inhomogeneous snow ablation, *Remote Sens.*, *7*(7), 8995–9019.

Little, R. L., D. L. Peterson, and L. L. Conquest (1994), Regeneration of subalpine fir (Abies lasiocarpa) following fire: Effects of climate and other factors, *Can. J. For. Res.*, *24*(5), 934–944.

Liston, G. E. (1999), Interrelationships among snow distribution, snowmelt, and snow cover depletion: Implications for atmospheric, hydrologic, and ecologic modeling, *J. Appl. Meteorol.*, *38*(10), 1474–1487.

Liston, G. E. (1995), Local advection of momentum, heat, and moisture during the melt of patchy snow covers, *J. Appl. Meteorol.*, *34*(7), 1705–1715.

Liston, G. E. (2004), Representing subgrid snow cover heterogeneities in regional and global models, *J. Clim.*, *17*(6), 1381–1397.

López-Moreno, J. I., S. R. Fassnacht, S. Beguería, and J. B. P. Latron (2011), Variability of snow depth at the plot scale: Implications for mean depth estimation and sampling strategies, *Cryosphere*, *5*(3), 617–629.

López-Moreno, J. I., J. Revuelto, M. Gilaberte, E. Morán-Tejeda, M. Pons, E. Jover, P. Esteban, I. Garcia, and J. W. Pomeroy (2014), The effect of slope aspect on the response of snowpack to climate warming in the Pyrenees, *Theor. Appl. Climatol.*, *117*(1–2), 207–219, https://doi.org/10.1007/s00704-013-0991-0.

López-Moreno, J. I., J. Revuelto, S. R. Fassnacht, C. Azorín-Molina, S. M. Vicente-Serrano, E. Morán-Tejeda, and G. A. Sexstone (2015), Snowpack variability across various spatiotemporal resolutions, *Hydrol. Processes*, *29*(6), 1213–1224, doi:10.1002/hyp10245.

Luce, C. H., D. G. Tarboton, and K. R. Cooley (1999), Sub-grid parameterization of snow distribution for an energy and mass balance snow cover model, *Hydrol. Processes*, *13*(12), 1921–1933.

Lundquist, J. D., and M. D. Dettinger (2005), How snowpack heterogeneity affects diurnal streamflow timing, *Water Resour. Res.*, *41*, W05007, doi:10.1029/2004WR003649.

Lundquist, J. D., and A. L. Flint (2006), Onset of snowmelt and streamflow in 2004 in the western United States: How shading may affect spring streamflow timing in a warmer world, *J. Hydrometeorol.*, *7*(6), 1199–1217.

Lundquist, J. D., S. E. Dickerson-Lange, J. A. Lutz, and N. C. Cristea (2013), Lower forest density enhances snow retention in regions with warmer winters: A global framework developed from plot-scale observations and modeling, *Water Resour. Res.*, *49*, 6356–6370, doi:10.1002/wrcr.20504.

Lundquist, J. D., M. Hughes, B. Henn, E. D. Gutmann, B. Livneh, J. Dozier, and P. Neiman (2015), High-elevation precipitation patterns: Using snow measurements to assess daily gridded datasets across the Sierra Nevada, California, *J. Hydrometeorol.*, *16*(4), 1773–1792, doi:10.1175/JHM-D-15-0019.1.

Marks, D., and J. Dozier (1992), Climate and energy exchange at the snow surface in the alpine region of the Sierra Nevada: 2. Snow cover energy balance. *Water Resour. Res.*, *28*(11), 3043–3054.

Margulis, S. A., G. Cortés, M. Girotto, and M. Durand (2016), A Landsat-Era Sierra Nevada Snow Reanalysis (1985–2015), *J. Hydrometeorol.*, *17*(4), 1203–1221.

McGuire, M., A. W. Wood, A. F. Hamlet, and D. P. Lettenmaier (2006), Use of satellite data for streamflow and reservoir storage forecasts in the Snake River Basin, *J. Water Resour. Plan. Manage.*, *132*(2), 97–110.

Micheletty, P. D., A. M. Kinoshita, and T. S. Hogue (2014), Application of MODIS snow cover products: Wildfire impacts on snow and melt in the Sierra Nevada, *Hydrol. Earth Syst. Sci.*, *18*(11), 4601–4615.

Mott, R., and M. Lehning (2010), Meteorological modeling of very high-resolution wind fields and snow deposition for mountains, *J. Hydrometeorol.*, *11*(4), 934–949, doi:10.1175/2010JHM1216.1.

Mott, R., M. Schirmer, and M. Lehning (2011), Scaling properties of wind and snow depth distribution in an Alpine catchment, *J. Geophys. Res.*, *116*, D06106, doi:10.1029/2010JD014886.

Olson, D. L., and D. Delen (2008), *Advanced Data Mining Techniques*, Springer, Berlin Heidelberg.

Painter, T. H., K. Rittger, C. McKenzie, P. Slaughter, R. E. Davis, and J. Dozier (2009), Retrieval of subpixel snow covered area, grain size, and albedo from MODIS, *Remote Sens. Environ.*, *113*(4), 868–879, https://doi.org/10.1016/j.rse.2009.01.001.

Painter, T. H., et al. (2016), The Airborne Snow Observatory: Fusion of scanning LiDAR, imaging spectrometer, and physically-based modeling for mapping snow water equivalent and snow albedo, *Remote Sens. Environ.*, *184*, 139–152.
Parajka, J., and G. Blöschl (2008), The value of MODIS snow cover data in validating and calibrating conceptual hydrologic models, *J. Hydrol.*, *358*(3), 240–258.
Prokop, A., and E. S. Procter (2016), A new methodology for planning snow drift fences in alpine terrain, *Cold Reg. Sci. Technol.*, *132*, 33–43.
Raleigh, M. S., and J. D. Lundquist (2012), Comparing and combining SWE estimates from the SNOW-17 model using PRISM and SWE reconstruction, *Water Resour. Res.*, *48*, W01506, doi:10.1029/2011WR010542.
Raleigh, M. S., K. Rittger, C. E. Moore, B. Henn, J. A. Lutz, and J. D. Lundquist (2013), Ground-based testing of MODIS fractional snow cover in subalpine meadows and forests of the Sierra Nevada, *Remote Sens. Environ.*, *128*, 44–57, doi:10.1016/j.rse.2012.09.016.
Revuelto, J., J. I. López-Moreno, C. Azorin-Molina, and S. M. Vicente-Serrano (2014), Topographic control of snowpack distribution in a small catchment in the central Spanish Pyrenees: Intra-and inter-annual persistence, *Cryosphere*, *8*(5), 1989–2006.
Revuelto, J., J. I. López-Moreno, C. Azorin-Molina, and S. M. Vicente-Serrano (2015), Canopy influence on snow depth distribution in a pine stand determined from terrestrial laser data, *Water Resour. Res.*, *51*, 3476–3489, doi:10.1002/2014WR016496.
Rice, R., R. C. Bales, T. H. Painter, and J. Dozier (2011), Snow water equivalent along elevation gradients in the Merced and Tuolumne River basins of the Sierra Nevada, *Water Resour. Res.*, *47*, W08515, doi:10.1029/2010WR009278.
Rittger, K., T. H. Painter, and J. Dozier (2013), Assessment of methods for mapping snow cover from MODIS, *Adv. Water Resour.*, *51*, 367–380, doi:10.1016/j.advwatres.2012.03.002.
Rochefort, R. M., R. L. Little, A. Woodward, and D. L. Peterson (1994), Changes in sub-alpine tree distribution in western North America: A review of climatic and other causal factors, *The Holocene*, *4*(1), 89–100.
Salomonson, V. V., and I. Appel (2004), Estimating fractional snow cover from MODIS using the normalized difference snow index, *Remote Sens. Environ.*, *89*(3), 351–360.
Schirmer, M., and M. Lehning (2011), Persistence in intra-annual snow depth distribution: 2. Fractal analysis of snow depth development, *Water Resour. Res.*, *47*, W09517, doi:10.1029/2010WR009429.
Schirmer, M., V. Wirz, A. Clifton, and M. Lehning (2011), Persistence in intra-annual snow depth distribution: 1. Measurements and topographic control, *Water Resour. Res.*, *47*, W09516, doi:10.1029/2010WR009426.
Schneiderbauer, S., T. Tschachler, J. Fischbacher, W. Hinterberger, and P. Fischer (2008), Computational fluid dynamic (CFD) simulation of snowdrift in alpine environments, including a local weather model, for operational avalanche warning, *Ann. Glaciol.*, *48*(1), 150–158.
Sexstone, G. A., and S. R. Fassnacht (2014), What drives basin scale spatial variability of snowpack properties in northern Colorado?, *Cryosphere*, *8*(2), 329–344.
Shamir, E., and K.P. Georgakakos (2007), Estimating snow depletion curves for American River basins using distributed snow modeling, *J. Hydrol.*, *334*(1), 162–173.
Sturm, M., and A. M. Wagner (2010), Using repeated patterns in snow distribution modeling: An Arctic example, *Water Resour. Res.*, *46*, W12549, doi:10.1029/2010WR009434.
Sold, L., M. Huss, M. Hoelzle, H. Andereggen, P. C. Joerg, and M. Zemp (2013), Methodological approaches to infer end-of-winter snow distribution on alpine glaciers, *J. Glaciol.*, *59*(218), 1047–1059.
Sumargo, E., and D. R. Cayan (2017), Variability of cloudiness over mountain terrain in the Western United States, *J. Hydrometeorol.*, *18*, 1227–1245,https://doi.org/10.1175/JHM-D-16-0194.1.
Tappeiner, U., G. Tappeiner, J. Aschenwald, E. Tasser, and B. Ostendorf (2001), GIS-based modelling of spatial pattern of snow cover duration in an alpine area, *Ecol. Modell.*, *138*(1), 265–275.
Venn, S. E., K. Green, C. M. Pickering, and J. W. Morgan (2011), Using plant functional traits to explain community composition across a strong environmental filter in Australian alpine snow patches, *Plant Ecol.*, *212*(9), 1491–1499.
Walters, R. D., K. A. Watson, H. P. Marshall, J. P. McNamara, and A. N. Flores (2014), A physiographic approach to downscaling fractional snow cover data in mountainous regions, *Remote Sens. Environ.*, *152*, 413–425.
Weiss, A. (2001), Topographic position and landforms analysis, in *Poster Presentation*, vol. 200, ESRI User Conference, San Diego, Calif.
Wilson, A. M., and W. Jetz (2016), Remotely sensed high-resolution global cloud dynamics for predicting ecosystem and biodiversity distributions, *PLoS Biol.*, *14*(3), e1002415, doi:10.1371/journal. pbio.1002415.
Winstral, A., and D. Marks (2002), Simulating wind fields and snow redistribution using terrain-based parameters to model snow accumulation and melt over a semi-arid mountain catchment, *Hydrol. Processes*, *16*(18), 3585–3603.
Winstral, A., D. Marks, and R. Gurney (2013), Simulating wind-affected snow accumulations at catchment to basin scales, *Adv. Water Resour.*, *55*, 64–79, doi:10.1016/j.advwatres.2012.08.011.
Zheng, Z., P. B. Kirchner, and R. C. Bales (2016), Topographic and vegetation effects on snow accumulation in the southern Sierra Nevada: A statistical summary from lidar data, *Cryosphere*, *10*(1), 257–269.